

S. B. L. Cebry¹, C.-Y. Ke^{1, 2}, and G. C. McLaskey¹

¹School of Civil and Environmental Engineering, Cornell University, Ithaca, NY, USA

² Department of Engineering Science and Mechanics, The Pennsylvania State University, University Park, PA, USA

Corresponding author: Greg McLaskey (gcm8@cornell.edu)

Key Points:

- Slip under high stress levels is driven by elastic stress transfer from induced aseismic slip, ruptured beyond the fluid pressurized region
- Slip under low stress levels was primarily driven by fluid injection and was limited by the extent of the fluid pressurized region.
- Regardless of background stress level, fluid injection first produced steady aseismic slip, then slow slip events, and dynamic rupture.

Key Words:

Induced seismicity, fluid injection, aseismic slip, laboratory experiments, background stress, initiation

Abstract

Fluid injection stimulates seismicity far from active tectonic regions, however the details of how fluids modify on-fault stresses and initiate seismic events remains poorly understood. We conducted laboratory experiments using a biaxial loading apparatus with a 3 m saw-cut granite fault and compared events induced at different background shear stress levels. Water was injected at 10 mL/min and normal stress was constant at 4 MPa. In all experiments, aseismic slip initiated on the fault near the location of fluid injection and dynamic rupture eventually initiated from within the aseismic slipping patch. When the fault was near critically stressed, seismic slip initiated only seconds after MPa-level injection pressures were reached and the dynamic rupture propagated beyond the fluid pressure perturbed region. At lower stress levels, dynamic rupture initiated hundreds of seconds later and was limited to regions where aseismic slip had significantly redistributed stress from within the pressurized region to neighboring locked patches. We find that slow slip initiated when local stresses exceeded Coulomb failure criteria, but initiation of dynamic rupture required additional criteria to be met. Even high background stress levels required aseismic slip to modify on-fault stress to meet initiation criteria. We also observed slow slip events prior to dynamic rupture. Overall, our experiments suggest that initial fault stress, relative to fault strength, is a critical factor in determining whether a fluid-induced rupture will “runaway” or whether a fluid-induced rupture will remain localized to the fluid pressurized region.

Plain Language Summary

Humans can create earthquakes on natural faults by injecting fluids underground, however details regarding what factors affect these earthquakes are not fully understood. We conducted laboratory experiments on 3 m blocks of rock that slip similar to a natural fault. Our experiments investigated how the initiation and overall size of earthquakes differed when fluid was pumped into a critically loaded fault (nearly ready to host an earthquake) versus a fault that was less critical. In the near-critical case, earthquakes occurred quickly and ruptured the entire fault. These earthquakes required fluid pressure to start the earthquake, but then were sustained by energy already present in the rock rather due to fluid pressure. However, when the fault was not critical, earthquakes could only initiate after fluid pressure caused silent slip to redistribute significant amounts of shear stress from within the fluid pressurized area to the surrounding areas. When stress had redistributed enough that the surrounding areas reached a critical state, an earthquake initiated, but it did not rupture very far and remained small. Our experiments agree with recently published computer simulations that illustrate how induced earthquakes are strongly affected by the levels of preexisting stress in the rock.

1 Introduction

The injection of fluids into the Earth—be it for CO₂ sequestration, enhanced geothermal systems (EGS), or oil and gas operations—is known to induce earthquakes (Ellsworth, 2013; Raleigh et al. 1976; Keranen et al., 2014). Minimizing induced seismicity requires an understanding of what causes a fault to begin to slip, the mechanisms driving the transition from aseismic to seismic slip (i.e., initiation of dynamic rupture), and how large the resulting seismic event will grow (i.e., how far dynamic rupture is sustained). These factors help inform the maximum event magnitude and potential for runaway ruptures. This study explores how background stress levels affect the initiation and termination of fluid-induced ruptures using a 3 m rock experiment.

Fluid injection field experiments on the decameter scale highlight the important role of induced aseismic slip in the initiation of induced seismicity. Results from Guglielmi et al., (2015a) show that fluid injection primarily induced aseismic slip. They observed microseismicity as a by-product of aseismic slip rather than directly induced by fluid injection. Villiager et al., (2021) observed four clusters of seismicity, one of which was triggered by aseismic slip. Aseismic slip redistributed stress between fracture planes which initiated a cluster of seismicity that was otherwise unaffected by fluid injection.

Modeling studies found background stress levels are important for the characterization of induced seismicity. Galis et al., (2017) used linear elastic fracture mechanics (LEFM) models to simulate induced events and found the rupture arrest and the transition to runaway rupture (the point at which rupture is fueled by the background stress on the fault rather than changes due to fluid injection) were governed by friction parameters and background fault stress state. In a similar study, Larochelle et al., (2021) presented a model that extended results from Guglielmi et al., (2015a) and found that low frictional strength

levels (relative to initial stress) promoted acceleration of slip to dynamic levels. Models created by Wynants-Morel et al., (2021) focused on aseismic slip and the resulting micro-seismicity. They found that background stress levels affected the extent and amplitude of induced aseismic slip. They highlighted the importance of increased shear stress caused by induced aseismic slip since they found the seismicity front follows the shear stress front rather than the fluid pressure front. Yang and Dunham, (2021) studied aseismic slip during fluid injection into a 2D velocity strengthening fault and accounted for coupled slip-induced porosity and permeability changes. Despite changes in flow properties, they found that fluid injection induced a steadily expanding aseismic slip front and the migration rate of the slip front was affected by background stress levels. When background stress levels were high (i.e., the fault was closer to failure) the aseismic slipping patch grew faster than at lower stress levels.

Laboratory studies have found that fluid injected directly onto the fault can induce slip and, in some cases, unstable, dynamic slip. In laboratory experiments on small, cm-sized samples (smaller than the critical nucleation length scale, h^*), the stability of the sample is primarily controlled by the stiffness of loading frame (Dieterich, 1978; McLaskey and Yamashita, 2017). Stiff loading systems result in stable sliding. Using a stiff loading system, Wang et al., (2020) found that fluid injection pressurization rate plays a more important role in induced slip than just injection pressure. Similarly, Scuderi and Collettini, (2018) studied the frictional properties of a slow slipping system and compared slip acceleration to rate-and-state frictional properties to conclude that heterogeneous fluid diffusion along the thickness of a gouge layer significantly affects slip behavior. Passelègue et al., (2018) looked at fluid injection into a tight fault. They studied the effect of fluid pressurization rate and, to a lesser extent, background stress levels to find that in the presence of significant stress heterogeneities, overall slip deviated from the expected Coulomb failure criteria. Cebry and McLaskey, (2021) injected fluid into a 760 mm-long plastic sample that was larger than h^* and found that the speed of induced slip (slow and aseismic versus fast and seismic) depended on both normal stress levels and injection rate. Li et al., (2021) related small-scale experiments to natural faults and found that background stress state plays an important role in determining the maximum moment magnitude.

In the current work, we aim to fill in the gap between modeling, small laboratory fault studies, and decameter scale field studies using a 3 m laboratory granite/granite fault. The sample is instrumented with arrays of sensors to directly observe the spatial distribution of slip and stress changes associated with fluid-induced slow and dynamic slip. Additionally, the sample is large enough that the observed slip behavior—fast versus slow slip, confined versus runaway ruptures—is largely independent of apparatus stiffness or sample boundaries.

In this paper, we will describe friction and the initiation and termination of rupture using a simplified framework based on linear slip weakening friction (e.g., Ida, 1972; Andrews, 1976) and LEFM (e.g. Galis et al., 2017). In this

framework, a fault has a peak frictional strength τ_{peak} , a residual frictional strength, τ_{residual} , and an initial stress, τ_0 . A fault patch will begin to slip if shear stress, $\tau \geq \tau_{\text{peak}}$ (Hubbert and Rubey, 1959), but the slip may be slow and aseismic. The initiation of dynamic rupture requires additional criteria to be met. For example, τ_0 may have to exceed τ_{peak} on a region that is at least as large as h^* (Dieterich et al., 1992; Rice, 1993; Uenishi and Rice, 2003). Additional initiation criteria with time-dependent and/or rate-dependent properties are also likely required (McLaskey, 2019; Guérin-Marthe et al., 2019; Kaneko et al., 2016; Kato et al., 1992).

Once dynamic rupture has initiated, we consider the rupture propagation and termination to be similar to a propagating crack using a LEFM framework (Svetlizky & Fineberg, 2014) where the “fuel” which sustains dynamic rupture is the fault overstress, $\tau_0 - \tau_{\text{residual}}$ (Ke et al., 2018) and rupture can be stopped a few different ways. It can “run out of fuel”, that is, the rupture propagates sufficiently far into a region where $\tau_0 < \tau_{\text{residual}}$ (Kammer et al., 2015; Ke et al., 2021). Or it can reach a “barrier” with high strength (large τ_{peak}) and/or high fracture energy (Bayart et al., 2016; 2018). A high-strength barrier may be the result of a geometrical heterogeneity such as a fault jog, stepover, high-normal-stress bump, or fault termination. A high fracture energy barrier would likely be the result of a rheological change such as a shear zone composed of velocity strengthening minerals (i.e., clays (Ikari et al., 2009)).

Considering the LEFM framework described above, injection of fluid affects the conditions under which slip begins, dynamic rupture initiates, and slip (aseismic or dynamic) terminates. When fluid is injected into a fault or shear zone, it increases pore fluid pressure, P^f , in a region we term the pressurized zone. An increase in P^f decreases effective normal stress, $\sigma_{n, \text{effective}}$. Assuming a simplified Coulomb friction model (Byrelee, 1967), lower effective normal stress decreases τ_{peak} and τ_{residual} , but does not affect τ_0 . Lowering τ_{peak} such that $\tau_{\text{peak}} \leq \tau_0$ will cause slip to begin. Lowering τ_{peak} in a large enough region, or at a fast enough rate, can cause dynamic rupture to initiate. Lowering τ_{residual} provides more fuel for sustaining dynamic rupture. However, if the pressurized zone is small, this will do little to affect the overall size of the rupture.

In this study we loaded a 3 m long granite/granite fault to three different τ_0 levels relative to estimated friction strength τ_{peak} and τ_{residual} while applied normal stress was held constant. We then injected water directly onto the fault at a constant rate and allowed the water to diffuse freely. Strain and slip were measured at sixteen points along the fault. Our sensor spacing was 0.2 m, while nucleation length scale $h^* = 0.5 - 1$ m. This allows us to obtain detailed resolution of the nucleation process when the fault is perturbed by the injection of fluids at high pressure. In each case, fluid injection caused aseismic slip at the location of fluid injection, and after continued injection, slip accelerated to dynamic speeds. In the case of high τ_0 , the transition from stable to dynamic slip occurred just a few seconds after high injection pressures were achieved. In the case of low τ_0 , the transition to dynamic slip did not happen until hundreds of seconds later.

In all cases, aseismic slip redistributed shear stress to neighboring fault patches until the fault was favorable for rupture. However, the extent and amplitude of stress redistribution required was significantly more in the low background stress case.

In agreement with previous studies, we found that τ_0 strongly influenced the resulting induced seismicity. Once dynamic slip initiated, high τ_0 provided ample fuel for runaway rupture beyond the pressurized region since $\tau_0 > \tau_{\text{residual}}$. Low τ_0 required significant stress redistribution from aseismic slip for rupture to initiate, and then it was confined to the region perturbed by fluid-induced stress changes.

Unique from the modeling studies, we found that though slip begins when local τ_0 exceeds τ_{peak} , initiation of dynamic slip requires more stringent conditions. In all cases aseismic slip occurred prior to the initiation of dynamic slip, which suggests that this slow slip, or the ensuing elastic stress redistribution, was required for the dynamic event to fully initiate, even when τ_0 was high.

We used a numerical model (calibrated with an experimental shut-in test as described in Section 4) to estimate the extent of the fluid-pressurized region during the injection in our experiments. Those results indicate that, for high τ_0 , aseismic slip quickly expanded beyond the pressurized zone. For the case of low τ_0 , the aseismically slipping region more closely tracked the slow expansion of the fluid-pressurized zone. Regardless of whether aseismic slip exceeded the pressurized region or not, aseismic slip elastically redistributed shear stress from within the slipping region to locked fault patches that were otherwise unaffected by a change in fluid pressure. In the low τ_0 case, this elastic stress redistribution eventually allowed dynamic slip to initiate and rupture beyond the pressurized region, but was ultimately limited by the extent of elastic stress redistribution. In cases where τ_0 was initially above τ_{residual} , dynamic slip ruptured through the entire sample.

2 Experimental Methods

2.1 Apparatus and Sample

Two Barre granite blocks, collectively referred to as the sample, were loaded in a direct shear biaxial apparatus as shown in Figure 1. The moving block is 3.10 x 0.81 x 0.30 m (x, y, and z) and the stationary block is 3.15 x 0.61 x 0.30 m (x, y, and z). The simulated fault is a 3.10 m x 0.30 m interface in the x-z plane. The two sample halves were pressed together using an 18x2 array of hydraulic cylinders that apply a constant sample-average normal stress, τ_n , to the simulated fault in the y direction. Sample average shear stress, τ_{SA} , on the interface was applied in the positive x direction using a 6x3 array of hydraulic cylinders. The granite surfaces that make up the interface have been machined flat and a thin gouge layer has been allowed to build up through approximately 50 mm of slip during experiments on a dry granite/granite fault at an average normal stress of 7 MPa.

The fluid injection experiments presented in this paper were conducted on a wet fault surface. Water was first poured along the fault when it was held at a low sample-average fault normal stress, $\tau_n < 100$ kPa. This water was allowed to seep into the fault until water was observed on the bottom of the sample, indicating the water had penetrated the entire thickness of the sample. During the experiments, conducted at $\tau_n = 4$ MPa, a high-performance liquid chromatography (HPLC) pump was used to inject water at a constant rate through a 0.01 m diameter hole in the stationary block directly onto the fault at 0.15 m depth, and 2.33 m from the forcing end as described in Figure 1d. An additional 0.40 x 0.01 (x and z) trough was cut into the face of the stationary block. This trough was connected to another well and used as a monitoring well to measure water pressure on the fault during experiments. In a separate experiment, the trough was used to conduct a shut-in test to determine hydraulic properties of the fault. The top, bottom, and sides of the fault interface were left open to atmospheric pressure.

2.2 Instrumentation

Fluid pressure in the injection well and monitoring trough were measured using Omega PX309 series pressure transducers. τ_n and τ_{SA} were calculated from hydraulic pressure measured in the 18x2 and 6x3 array of cylinders, respectively. Precision of pressure measurements was ~ 1 kPa. Eddy current displacement sensors were used to measure local fault slip along the top of the simulated fault at 16 locations (E1-E16) as shown by the colored squares in Figure 1b. These sensors measure displacement (0.15 micron precision), between a probe glued to the stationary block and a target glued to the moving block. Local shear strain was measured using 16 semiconductor strain gauge pairs (S1-S16) glued 7 mm from the simulated fault on top of the moving block (colored circles in Figure 1b). Strain was converted to stress assuming a shear modulus of 30 GPa. Strain gauges and associated exposed wiring were covered in wax to prevent them from getting wet and electrically shorting due to the injected water that occasionally leaked out of the top trace of the fault.

Data from pressure and displacement sensors were recorded continuously at 50 kHz on a 20-channel digitizer then averaged to 5 kHz to reduce high-frequency noise. The strain data was simultaneously recorded at 1 MHz. The continuous strain data was then averaged to 1 kHz while a 1 s window of data around each stick-slip event was averaged to 100 kHz.

2.3 Experimental Procedure

Table 1 lists a summary of three experiments reported here. All experiments were conducted by applying $\tau_n = 4$ MPa, held approximately constant for the duration of the experiment by simply closing a valve. At the beginning of the experiment, to establish the strength levels τ_{peak} and $\tau_{residual}$, we created three sample-spanning dynamic rupture events (“complete-rupture” stick-slip events) by manually pumping fluid into the 6x3 array of hydraulic cylinders, at a rate of roughly 0.03 MPa/s. These events, triggered solely by an application of

externally applied shear stress are referred to as “shear-triggered” events. After three events, τ_{SA} was increased to a prescribed level, τ_0 , and held constant. Then, water was injected directly into the fault at a constant rate, Q , of 10 mL/min. Slip events that occurred due to an increase in fluid pressure are referred to as “fluid-triggered” events. Experiments were conducted with water, apparatus, and samples at approximately 21°C and ambient room humidity.

3 Experimental Results

3.1 Summary

Figure 2 shows the experimental data from Case A (high τ_0 , orange), B (moderate τ_0 , green), and C (low τ_0 , blue) overlaid for comparison. The data is time shifted so the peak injection fluid pressure is at $t = 0$. Slip and shear stress measurements, measured by sensors located at the top of the sample, are offset by the sensor location along the fault. τ_0 was set to various levels at the start of experiments, as shown by the different τ_{SA} levels at $t = -5$ s. Fluid injection began approximately 140 to 200 s prior to peak injection pressure. \mathbf{P}^f is measured within the injection well (cross-sectional area of 3.14 cm²) at the center of the fault (note the difference in measurement locations of fluid injection pressure and slip/strain sensors, see Section 5.1 for additional details). All experiments reach a similar peak injection pressure, $\mathbf{P}_{\max}^f = 7.2 \pm 0.1$ MPa and followed a similar trend as pressure built up to \mathbf{P}_{\max}^f , followed by a 2 MPa drop in fluid pressure. The top, bottom, and sides of the sample were left open to atmospheric pressure during experiments, so we expect this drop happened when the fluid reached one of the fault edges and was able to escape.

Fluid injection resulted in aseismic and dynamic slip and local stress changes in all cases. In Figure 2 gradual increases in slip coincident with gradual changes in local shear stress indicate aseismic slip (i.e., Case C for time window shown). Sudden increases in slip at the same time as sudden drops in local shear stress indicate dynamic rupture events (i.e., Case B, $t = 15.3$ s). If the dynamic rupture event ruptured through the forcing end of the sample (i.e., dynamic ruptures in Case A and B), events had an associated drop in τ_{SA} .

Figure 3 shows the spatio-temporal evolution of local shear stress changes overlaid on a colormap of slip rate to highlight how the fault transitioned from locked to dynamic rupture for each of the three cases. Top panels show slip rate and stress for the duration of fluid injection (note the different time scales). Middle panels show the same data from 0.5 s before to 3 s after \mathbf{P}_{\max}^f to compare the initial growth of induced aseismic slip on a uniform time scale. Bottom panels show a single fluid-triggered dynamic event for each case on a uniform time scale for comparison to show the rupture speed and extent.

In each of the three cases, slip starts in the center of the sample at $x = 2.3$ m, closest to the point of fluid injection, which is indicated by the blue faucet (Figure 3d, e, f). In all cases, induced slip began within one second of \mathbf{P}_{\max}^f and started as a small patch of aseismic slip which slipped in an episodic manner. The timing, slip rate, and rupture speed of the aseismic slip and episodic slip

varied for each case, however the location was generally consistent. Case A (high σ_0) began to slip aseismically earlier (0.1 s before \mathbf{P}_{\max}^f) than Case B (moderate σ_0) or C (low σ_0) (0.2 s and 0.3 s after \mathbf{P}_{\max}^f). In all cases aseismic slip was first measured at the sensor closest to the injection well (E12), then expanded bilaterally. The aseismic slipping patch expanded quicker in Case A (51 cm/s) than Case B or C (39 cm/s and 7.8 cm/s). In Case A the aseismic slipping patch grew to be 1.2 m long over approximately 1 s, whereas in Case B it took 5 s to reach 1.2 m long and in Case C it took 310 s. Episodic slip was more prevalent in Case A than Case B or C with distinct slow slip events starting less than a second after aseismic slip began (Figure 3d, e, and f). In Case A or B slow slip episodes occurred seconds apart and reached near dynamic slip rates (1.2 mm/s) while in Case C slow slip episodes occurred hundreds of seconds apart and reached a maximum slip rate of 16 mm/s.

Table 1 summarizes the experimental parameters for each of the three cases and shows the details of events within each case. “Total aseismic slip” refers to the total slip that occurred with slip rate, $\dot{\mathbf{D}}$, below 10 $\mu\text{m/s}$ from the start of fluid injection to just prior to the initiation of the dynamic slip event. Slip that exceeds 10 $\mu\text{m/s}$, such as the partial slip events A1 and B1, is excluded. Event C1 does not exceed 10 $\mu\text{m/s}$ and is included in total aseismic slip. Aseismic slip is measured using sensor E12 is located closest to the point of fluid injection and was always the sensor that measured the most slip. “Partial slip event” refers to the fastest slip event that did not rupture through the ends of the sample and occurred prior to a dynamic rupture (Events A1, B1, and C1). Partial rupture events have a rupture extent less than the sample length (3.1 m). Slip sensors that were spaced 0.2 m apart were used to determine the rupture length, which limited the resolution. “Dynamic slip event” refers to the largest dynamic rupture produced by fluid injection (Events A2, B2, and C2).

Table 1

Experimental Summary

		Case A	Case B	Case C
Overall experiment properties	$\bar{\sigma}$ (MPa)			
	σ_0 (MPa)			
	Q (mL/min)			
	\mathbf{P}_{\max}^f (MPa)			
Start of aseismic slip	\mathbf{P}^f (MPa) at start			
	$10 \text{ nm/s} < \dot{\mathbf{D}} < 10 \text{ } \mu\text{m/s}$			

		Case A	Case B	Case C
Total aseismic slip Induced slip with $\dot{D} < 10\mu m/s$	Start time relative to P_{\max}^f (s) Maximum slip ^{a, b} (m)			
	Peak Slip Rate ^a (m/s)	7.7e-5	9.1e-5	3.1e-5
	^{b, c}_{max} (MPa)	/+0.34	/+0.58	/+1.11
	Rupture extent (m)			
	Event name	A1	B1	C1 (aseismic)
Partial slip event Largest slip event that did not rupture through either end of the sample	P^f (MPa) Start time relative to P_{\max}^f (s) Maximum slip ^{a, b} (m)			
	Peak Slip Rate ^a (m/s)	3.0e-3	5.5e-3	3.1e-5
	^{b, c}_{max} (MPa)	/+0.08	/+0.09	/+0.82
	Rupture extent ^b (m)			

		Case A	Case B	Case C
Dynamic slip event	Event name	A2	B2	C2
Largest dynamic rupture event produced by fluid injection	P^f (MPa)			
	Start time relative to P^f_{max} (s)			
	Maximum slip^{a, b} (m)			
	Peak Slip Rate^a (m/s)			
	P^f_{max} (MPa)			/+0.40
	Rupture extent^b (m)	complete	complete	

^a Maximum measured by any slip sensor. ^b Measured over a 1 s window centered around the rupture event. ^c Negative values refer to the stress decrease within the slipped region and positive values refer to increases in shear stress on locked sections of the fault.

The largest slow slip event in each case (Events A1, B1, and C1 shown in Figure 3) significantly increased the size of the aseismic slipping patch and resulted in a significant change in shear stress. These events are partial slip events, meaning they only ruptured part of the fault, while both ends of the sample remained locked. Event B1 slipped fastest, followed by Event A1 then C1. However, Event B1 slipped less than A1. Event C1 slipped more than A1 or B1 despite slipping significantly slower. The start and end of Event C1 was less well-defined than A1 or B1 since it accelerated and decelerated very gradually. Details of these events are listed in Table 1.

In each case, dynamic events (Events A2, B2, and C2) initiated from within the slow slipping patch (ex. Figure 3g from 3.22 to 3.24 s at 1.9 m from the forcing end). In event A2 and B2, dynamic rupture propagated along the entire length of the fault. Event C2 only ruptured a portion of the fault from 0.2 m to 3.1 m, leaving part of the fault, from 0.0 m to 0.2 m locked (Figure 3i). Event C2

was slower and slipped less than A2 or B2. Details of these events are listed in Table 1.

3.2 Changes in σ due to aseismic and seismic slip

With continued injection and time, the slipping patch and fluid pressurized region grew. This decreased shear stress in the slipped region and increased shear stress on the surrounding locked patches, as shown in Figure 4. Figure 4a shows the change in stress from the start of fluid injection to just prior to dynamic rupture, while Figure 4b shows the change in stress due to dynamic rupture (Events A2, B2, C2). Fluid injection at $x = 2.3$ m resulted in decreased shear stress while the surrounding locked region increased in shear stress. This occurred because in each case induced aseismic slip prior to dynamic rupture elastically redistributed shear stress, creating a shear stress concentration beyond the point of fluid injection. The edge of the sample (3 m) did not see a significant increase in stress since it was allowed to release stress through the free surface. In Case A, this stress redistribution was small, and in Case C, a more significant redistribution of stress was observed. Some areas saw an increase of more than 1 MPa over hundreds of seconds.

Both aseismic and dynamic slip had associated stress changes, but aseismic slip always caused a greater stress change than dynamic slip. This is illustrated particularly well in Case C. Event C1 occurred at 2 s reached a maximum slip rate of 1.5×10^{-5} m/s and caused a 1.2 MPa decrease in stress close to the point of fluid injection at $x = 2.3$ m (Figure 4a). In comparison, Event C2 occurred at 513 s which reached a maximum slip rate of 2.5×10^{-3} m/s and caused a 0.2 MPa decrease in stress just outside of the pressurized zone at 1.75 m (Figure 4b). These events are partial slip events so local shear stress on the slipped section of the fault decreased, while shear stress on locked sections of the fault increased (Figure 3i). Similar results were seen in Case A and B (Figure 4b).

3.3 Determination of stress and strength levels

To better interpret the results described above, we estimated the spatial distribution of stress and strength (σ_0 , σ_{peak} , and $\sigma_{residual}$) from local measurements of shear strain from 16 strain gauge pairs, as shown in Figure 5. σ_0 was measured just prior to the start of fluid injection and σ_{peak} , and $\sigma_{residual}$ measurements were made from complete-rupture “shear-triggered” stick-slip events generated tens of seconds prior to the start of fluid injection. Figure 5a and b show an example shear-triggered slip event measured on all 16 strain gauge pairs. Figure 5c shows a single strain gauge pair from the same event over a shorter time window to demonstrate how σ_{peak} , and $\sigma_{residual}$ were determined.

σ_{peak} is the maximum shear stress on the fault during the shear-triggered slip event. This peak can come from an increase in sample-average shear stress (Figure 5a and b, S1), a local stress change from a propagating rupture (Figure 5a and b, S15), or a decrease in normal stress. Once a section of the fault reaches peak shear stress, that section begins to slip and shear stress is reduced to a minimum, referred to as $\sigma_{residual}$. In this study, $\sigma_{residual}$ is taken from

the first stress drop which is associated with the primary rupture in the event. Secondary ruptures or reflected shear waves may decrease the final shear stress even further beyond τ_{residual} (overshoot) (Kanamori and Rivera, 2006) or may increase stress above τ_{residual} (undershoot) (Madariaga, 1976). In our analysis we do not consider overshoot or undershoot and only consider τ_{residual} calculated before the rupture propagates to the end of the sample.

We calculated τ_{peak} and τ_{residual} for each of the three complete-rupture shear-triggered events generated prior to fluid injection in Case A, B, and C. Figure 5d shows an example comparison of τ_{peak} for three events prior to Case A experiments. These values were found to be consistent to within ± 0.23 MPa across multiple events within the same run despite differences in initiation location (Event 1 initiated around 2.1 m and Events 2 and 3 initiated around 0.5 m). Similar results were seen for τ_{residual} and for Case B and C. τ_{peak} and τ_{residual} measurements were found to be consistent to within ± 0.45 MPa across the three cases (A, B, and C) which were conducted as separate experimental runs on the same day (Figure 5e). This variation in τ_{peak} and τ_{residual} strength estimates is shown by the grey shaded region in Figure 5f and g and compared to τ_0 measured prior to fluid injection for the three cases. Despite the large uncertainty, these values illustrate the background stress levels, relative to τ_{peak} and τ_{residual} as a function of distance along the fault.

The relative distribution of τ_0 as a function of distance along the fault shown in Figure 5f and g illustrates how close each case was to a critically stressed condition at the start of fluid injection. Figure 5f shows shear stress (relative to a zero-measurement made at the beginning of the day when the sample was minimally stressed) as a function of distance along the fault and Figure 5g shows the same data normalized by the average τ_{peak} from all three cases. τ_{peak} and τ_{residual} are taken as the average value from three shear-triggered stick-slip events at the beginning of each experiment. τ_0 is the shear stress measured just prior to fluid injection. For Cases A and B, $\tau_{\text{peak}} > \tau_0 > \tau_{\text{residual}}$ at all locations along the fault. For Case C, $\tau_0 < \tau_{\text{residual}}$ for most of the fault.

In all cases, the absolute stress level varied along the length of the fault due to an uneven normal stress distribution that naturally occurred on this apparatus (Ke et al., 2018, Figure 3f). In the experiments presented in this paper, frustrated Poisson stresses built up from an increase in normal stress had been relieved prior to fluid injection by multiple complete-rupture events. The distribution of shear stress tended to match the distribution of normal stress, since the fault was approximately uniformly critically stressed and all points on the fault follow Coulomb failure criteria. This resulted in regular sets of complete-rupture shear-triggered rupture events, unlike the ‘‘Poisson’’ experiments reported previously (Ke et al., 2018, Wu and McLaskey, 2019, McLaskey, 2019), where the initial shear and normal stress distribution were uneven and varied from event to event. During fluid injection, the normal stress on the fault was constant in time, although non-uniform in space.

4 Hydraulic Diffusivity from a Shut-in Test and Numerical Model

The injection trough was used to perform a shut-in test to constrain fault diffusivity. Results from the shut-in test were matched to a 2D diffusion model (Figure 6). Monitoring wells were used in later experiments to measure fluid pressure 56 cm from the edge of the injection well and supported the findings from the shut-in test. To perform the shut-in test, water was injected into a wet, but unpressurized fault and was allowed to build up pressure. Once the injection well pressure began to increase rapidly and reached MPa-level pressures, injection was stopped. Pressure in the well decreased as fluid diffused along the fault.

To match the injection well pressure decay results, a finite-difference model was created to match experimental measurements to diffusion parameters using a 2D diffusion equation $\frac{\partial P}{\partial t} = \alpha(\frac{\partial^2 P}{\partial x^2} + \frac{\partial^2 P}{\partial y^2})$. In this equation, P is the fluid

pressure and the hydraulic diffusion coefficient is $\alpha = \frac{k}{\beta_c v}$, where k is the fault permeability, β_c is the storage coefficient, and v is the fluid’s dynamic viscosity. Initial and boundary conditions in the model were set to match experimental measurements (Figure 6a). The edges of the fault were modeled using a Dirichlet boundary condition with an imposed pressure of 0 MPa, since they were open to atmospheric pressure during experiments. For computational efficiency, a symmetry boundary condition was used along the x and y centerline of the fault. Initially the fluid pressure on the modeled fault was zero. After time zero, experimental pressure measurements made at the injection trough were imposed as a boundary condition in the injection region, modeled as an area representing the size and location of the experimental injection trough. At 120 s the imposed boundary condition at the injection region was removed and replaced with a symmetry boundary condition on $x = 0$ m and $y = 0$ m (purple lines in Figure 6a) and a diffusion boundary condition on $x = 0.1$ m and $y = 0.01$ m (dashed lines in Figure 6a). The pressure in the injection region was allowed to freely decrease as pressure diffused away from the shut-in injection trough. α was varied to match the modeled pressure decay to the experimental measurements. The model with $\alpha = 1 \times 10^{-5}$ m²/s best matched the experimental pressure decay in the injection well in terms of both shape and magnitude (Figure 6b). Modeled injection well pressure with $\alpha = 1 \times 10^{-6}$ m²/s and $\alpha = 1 \times 10^{-4}$ m²/s are shown in Figure 6b for comparison. We did not consider any coupled poromechanical behavior such as changes in permeability due dilation or compaction from changes in effective normal stress or slip in this model.

The hydraulic diffusivity of the laboratory fault was found to be consistent with previous studies of granite/granite faults but lower than faults in permeable rocks such as sandstone or fault zones at shallow depths. Other granite laboratory faults have been measured to have diffusion coefficients of 10^{-5} m²/s (Passelegue et al., 2018) and 7.5×10^{-5} m²/s (Bartlow et al., 2012) and corresponding permeabilities of 5×10^{-14} to 3×10^{-16} m² (Bartlow et al., 2012) and 7.895×10^{-17} (Kranz et al., 1979). Diffusivity of faults at shallow depths, typically targeted for fluid injection, varies but is typically on the order of 10^{-1} to

$10^{-2} \text{ m}^2/\text{s}$ (Bhattacharya and Viesca, 2019; Goebel and Brodsky, 2018).

5 Discussion

5.1 Differences in measurement locations

It is worth noting that we compare slip measurements on the top of the sample to fluid pressure measured at the center of the fault, at 0.15 m depth. This results in some discrepancies in the timing of slip compared to the timing of peak fluid pressures (i.e., Figure 2). We expect that slip begins when Coulomb failure criteria is exceeded, however we cannot measure fault slip until the slipping patch has grown to the depth of the sample (0.3 m).

Similarly, overpressures at the injection point are measured, but we cannot directly compare them to slip or local stress measurements made on the top of the sample. Since the diffusivity of the fault is very low and sample sides are open to atmospheric pressure (See Section 4), it is likely that only a small section of the fault (likely 7.1 cm^2 based on the diffusion model described in Section 4) has exceeded sample average normal stress when peak fluid pressure is reached, suggesting that the overpressures only affected a very small portion of the fault, far from sensor measurements.

5.2 Growth of aseismic slip patch

In our experiments, the expansion of fault slip outpaced that of the fluid pressurized region in high stress cases and was driven by elastic stress transfer from the aseismic slip front. Figure 7 compares the extent of the fluid pressurized region with slip rate (a, b, c), change in shear stress, and cumulative slip (d, e, f). Due to the limited number of slip measurements along the fault, the expansion of the slow slipping region appears jagged and stair stepped (ex. Figure 7a, from 0 to 1 s), but based on smooth slip and strain measurements we believe the slow slipping region expanded smoothly and continuously. It only expanded suddenly and rapidly when a slow slip event or dynamic slip occurred, as indicated in Figure 8b. In Case A and B, the aseismic slip patch expanded quickly (510 mm/s and 390 mm/s, respectively) and outpaced the pressurized region. In Case C, slip expanded slower (78 mm/s), and the extent of slip more closely tracked the fluid pressurized region. Wynants-Morel et al., (2020) observed similar expansion rates from computational models, ranging from 25 to 420 mm/s depending on background stress levels. Yang and Dunham, (2021) found modeled expansion rates to vary from 0.12 to 12 mm/s and found a correlation between expansion rate and background stress. In-situ measurements based on seismicity migration range from $12 \text{ }\mu\text{m/s}$ in Cahuilla, California (Ross et al., 2020) to 12 mm/s in the Yellowstone caldera (Shelly et al., 2013). In all cases, aseismic slip created a region of increased shear stress beyond the area affected by fluid pressure. In agreement with previous modeling studies (Gargash and Germanovich, 2012; Yang and Dunham, 2021), we conclude that in high stress cases, slip can quickly outpace fluid pressure, but in low stress cases aseismic slip cannot be sustained beyond the fluid pressurized region.

Episodic slow slip events and seismic slip events assisted with the expansion of the aseismic slip patch. In all cases slow slip periodically accelerated and began to expand more rapidly, then decelerated without reaching dynamic slip rates or radiating detectable seismic waves. We refer to this acceleration and deceleration as an episodic slow slip event. Episodic slow slip events have been observed in other laboratory experiments (McLaskey, 2019, Figure 4d) on a dry fault. Both episodic slow slip (Figure 3, Events A1, B1, and C1) and seismic slip (Figure 3, Events A2, B2, and C2) initiated within the aseismic slipping patch and had a larger extent than the aseismic slip patch, resulting in an expansion of the aseismic slip patch. Both also caused significant changes in shear stress which promoted larger subsequent events. Seismic slip resulted in sudden changes in slip rate, slip extent, and stress, while episodic slip caused more gradual changes.

5.3 Initiation of dynamic slip

A close look at the slip measurements for the different cases highlights the variability of the dynamic rupture initiation process. Figure 8 provides an image of spatio-temporal evolution of the initiation of slip and compares a 1 s window of slow and fast events generated under different stress cases. Each line represents a snapshot of the slip distribution along the fault relative to slip at the beginning of the time window. As a result, lines that are spaced further apart indicate fast slip (>1 mm/s) while closely spaced lines that show the pink-purple color banding indicate slow slip ($\mu\text{m/s}$).

Dynamic rupture events (Figure 8a, e, f, g, h) initiated from a region of the fault that was actively slow slipping ($1 - 10 \mu\text{m/s}$), which can be considered the nucleation region. For example, Figure 8f shows that dynamic rupture (Event A2) initiated from the left edge of a 1.4 m slow slipping patch (from 1.7 to 3.1 m). Figure 8g (Event B2) shows a similar example. In general, the initiation of these events is quite similar to initiation observations on the same sample under dry conditions without fluid pressure (McLaskey, 2019). However, fluid-triggered events show nucleation regions that are $\sim 50\%$ larger than the nucleation regions of shear-triggered events (Figure 8a, Figure 8e), likely because the low $\sigma_{n, \text{effective}}$ caused an increase in h^* . In contrast, Event C2, shown in Figure 8h, initiated more abruptly from within a 1.5 m nucleation region without much indication of slip acceleration or expansion of the nucleation region. This is unexpected since Event C2 likely had a larger fluid-pressurized region which would theoretically increase h^* compared to Events A2 and B2 (Figure 8f, Figure 8g). However, McLaskey (2019) illustrated many cases where initiation occurred far more abruptly than expected, and this resulted from sudden initiation on a stuck patch or increases in loading rate after a “hold” period. Other studies also described how complicated initiation processes can result from fault strength heterogeneity (Cattania and Segall, 2021) or local loading rate perturbations (Kaneko et al., 2016; McLaskey and Kilgore, 2013; Kato et al., 1992).

5.3.1 Successful initiation under low τ_0 conditions

In Case C, the fault was initially neither favorable for slip nor dynamic rupture. Case C required continued fluid injection and stress redistribution from induced aseismic slip to both initiate and sustain dynamic rupture (Event C2). Even then, Event C2 initially only propagated along areas of the fault where elastic stress transfer from aseismic slip increased shear stress levels above τ_{residual} (1.3 – 2.0 m, shown in Figure 4a) or fluid pressure had lowered $\sigma_{n, \text{effective}}$. The C2 rupture front stopped at $x = 1.2$ m once it ruptured beyond the region of stress change, then it restarted again once the other edge of the rupture had propagated through the leading edge of the sample, before it finally terminated 0.2 m from the forcing end (Figure 3i and Figure 8h). Nucleation requirements were met but rupture stopped once it propagated into a region where $\tau_0 \leq \tau_{\text{residual}}$ and the dynamic rupture could not be sustained. This suggests that injection into a low τ_0 fault system is not limited to aseismic slip but can also induce dynamic events that are ultimately confined to the fluid-perturbed region.

5.3.2 Failed initiation under high τ_0 conditions

Case A was highly stressed and aseismic slip began just before P_{max}^f was reached. However, despite the high τ_0 , the slipping patch was initially unable to meet initiation criteria, which prevented dynamic rupture at first. Event A1, shown in Figure 8b occurred under near critical stress conditions ($\tau_0 > \tau_{\text{residual}}$, Case A in Figure 5f and g) but only ruptured a portion of the fault. Slip rate remained just below dynamic levels and the event slowed rather than accelerating into a dynamic event, so we conclude that dynamic rupture initiation criteria were not met. Only the fluid-pressurized region (~ 0.2 m, Figure 6d) was favorable for slip initiation ($\tau_0 = \tau_{\text{peak}}$) and this was apparently not enough to initiate dynamic rupture. It was not until the aseismic slipping patch grew and the associated stress redistribution loaded neighboring fault patches that a dynamic event was able to initiate and rupture the entire fault (Event A2, Figure 8f).

The details behind why dynamic rupture did not initiate in Event A1 are not completely understood. The fault was sufficiently stressed to sustain dynamic rupture as evidenced by Event A2 which occurred a short time later. Yet, something inhibited slip from accelerating in Event A1. Dilatancy may play a role; as slip accelerates the fault dilates, reduces fluid pressure, and increases effective normal stress and strengthens the fault, thus inhibiting dynamic rupture. However, slow slip events can occur on dry faults (Leeman et al., 2016; McLaskey and Yamashita, 2017), and a similar slow slip oscillation was observed just prior to dynamic rupture on the same sample under dry conditions, as reported in McLaskey (2019), Fig. 4d, so the differences in A1 and A2 are not entirely due to fluid-related dilatancy effects. It is also possible that the dynamic rupture initiation process was strongly affected by a locally heterogeneous pressure, strength, and permeability due to asperities in both x and z directions, which have been exhibited through grooves on the laboratory fault surfaces (Brodsky et al., 2020).

5.4 Driving mechanism varies based on background stress levels

The driving force behind induced seismicity differs between the high τ_0 and the low τ_0 cases: high τ_0 cases were primarily driven by elastic stress transfer while low τ_0 cases were primarily driven by fluid injection (Figure 9).

When $\tau_0 > \tau_{\text{residual}}$, the aseismic slip patch quickly outpaced the fluid pressurized region, elastically redistributed shear stress, and primed the fault for initiation of dynamic slip. Once a dynamic event was initiated, there was ample fuel for the rupture to propagate along the entire fault (Figure 9a). The fluid pressurized region did not significantly increase over the duration of slip, aseismic or seismic, (Figure 7a) suggesting that elastic stress transfer was the primary driving force. In cases with high τ_0 , fluid pressure perturbation was only needed to meet initiation criteria for dynamic rupture. We also observed that local stress changes associated with aseismic slip were always greater than stress changes associated with dynamic slip in our experiments.

When $\tau_0 < \tau_{\text{residual}}$, growth of the aseismic slipping patch more closely matched the growth of the fluid pressurized region (Figure 7c). Expansion of aseismic slip was fueled by continued injection rather than strain energy stored in the fault rocks (Figure 9b). Similarly, dynamic rupture was limited by the extent of the fluid pressurized zone and region affected by fluid-induced aseismic slip. This suggests that slip was primarily driven by fluid injection.

This difference in driving mechanisms was also observed by Wynants-Morel et al., (2021) who saw a marked difference in the migration velocity of seismic events depending on if the aseismic slip front or fluid pressure front was driving the observed seismic events. Similar to

our experiments, they observed the transition from injection-driven to stress-driven front propagation occurred when background shear stress was above residual shear stress.

5.5 Relation to observed seismicity

These experiments provide insight into the observations of induced seismicity on natural faults. Case A relates to injection into a high τ_0 region near a fault that is ready to sustain dynamic rupture and only needs to initiate a dynamic event. This situation will produce large dynamic events, with few small events such as the events that occurred in 2017 in Pohang, South Korea (Kim et al., 2018; Langenbruch et al., 2020). Initiation is controlled by fluid injection, but once initiated, event size is limited by the presence of fault geological or rheological barriers, rather than the extent of a fluid pressurized region.

Case C relates to injection into a low τ_0 region. The fault is not favorable for dynamic rupture and results in predominantly aseismic slip. The low stress case may help explain field experiments of Guglielmi et al., (2015a). Micro seismicity was triggered, likely due to fault heterogeneities, but the bulk of deformation was aseismic (Cappa et al., 2019; Guglielmi et al., 2015b, and the expansion of the slow slipping region was inferred to be slow (cm/s, Guglielmi et al., 2015b). Another contributing factor was likely a large h^* due to low normal stress and

velocity dependent frictional properties, and as a result, the slipping patch never grew large enough or fast enough to initiate dynamic rupture (Cappa et al., 2019). The low τ_0 explanation matches results from Larochelle et al., (2021) who found that models with $\tau_0 < \tau_{\text{residual}}$ best matched experimental measurements. Although slip may have been able to propagate beyond the pressurized region, its expansion was ultimately controlled by fluid injection-induced stress changes and was largely confined to the fluid-perturbed region, preventing the slipping patch from reaching h^* .

6 Conclusions

Background stress on the fault, relative to fault strength levels, is a critical factor in determining both the ease at which earthquakes are initiated and the extent of their rupture. We conducted laboratory experiments with direct fluid injection at various τ_0 levels. All cases resulted in induced aseismic slip followed by dynamic slip. At high τ_0 this aseismic slip was necessary to initiate dynamic slip, but once initiated, the fault was sufficiently stressed to produce a “runaway” dynamic rupture that was sustained by initial stress rather than fluid-induced stress changes. At low τ_0 , significant amounts of aseismic slip, driven by fluid injection, were required to modify the fault stress state before the fault was favorable to initiate or sustain dynamic rupture. The start of slip, initiation of dynamic rupture, and rupture extent were controlled by fluid injection. In this case, rupture size was controlled by the fluid injection since it arrested soon after it propagated outside of the fluid perturbed region. Most of our observations matched expectations from modeling studies. For example, the expansion of the aseismic slip patch was faster in high τ_0 cases and slower in low τ_0 cases. In high τ_0 cases, aseismic slip quickly outpaced the diffusing fluid pressure front but it more closely matched the fluid pressure front in low τ_0 cases. Based on differences in aseismic slip expansion and dynamic rupture termination, our observations support Wynants-Morel et al. (2021) who proposed that induced slip is primarily driven by elastic stress transfer when $\tau_0 > \tau_{\text{residual}}$ and fluid injection when $\tau_0 < \tau_{\text{residual}}$.

However, the details of dynamic rupture initiation observed in our experiments paint a more complicated picture. In our experiments, fluid injection initially produced slow slip events that accelerated beyond background slip rates, but failed to initiate dynamic slip, even under high τ_0 conditions. Fluid induced slow slip events did cause rapid expansion of the slow slipping region. On the other hand, under low τ_0 , dynamic rupture was able to initiate rather abruptly and unexpectedly from within the fluid perturbed region. The nucleation of dynamic rupture is complex, likely because stress heterogeneity introduced by fluid injection, loading rate effects, and other nuanced nucleation criteria are important in fluid injection, as the fault is unevenly loaded by fluid pressure and elastic stress transfer.

Acknowledgments

This work was supported by National Science Foundation Grant EAR- 1847139.

Data used in this paper were acquired during laboratory experiments conducted at Cornell University.

Open Research

Data reported here are publicly available online (<https://eCommons.cornell.edu>).

References

- Andrews, D. (1976). Rupture Velocity of plane strain shear cracks. *J Geophys Res*, 5679-5687. doi:10.1130/0016-7606(1959)70[115:ROFPIM]2.0.CO;2
- Bartlow, N., Lockner, D., & Beeler, N. (2012). Laboratory triggering of stick-slip events by oscillatory loading in the presence of pore fluid with implications for physics of tectonic tremor. *Journal of Geophysical Research B: Solid Earth*, 117(11). doi:10.1029/2012JB009452
- Bayart, E., Svetlizky, I., & Fineberg, J. (2016). Fracture mechanics determine the lengths of interface ruptures that mediate frictional motion. *Nature Physics*, 12(2), 166-170. doi:10.1038/nphys3539
- Bayart, E., Svetlizky, I., & Fineberg, J. (2018). Rupture Dynamics of Heterogeneous Frictional Interfaces. *Journal of Geophysical Research: Solid Earth*, 123(5), 3828-3848. doi:10.1002/2018JB015509
- Bhattacharya, P., & Viesca, R. (2019). Fluid-induced aseismic fault slip outpaces pore-fluid migration. *Science*, 364(6439), 464-468. doi:10.1126/science.aaw7354
- Brodsky, E. E., McLaskey, G. C., & Ke, C.-Y. (2020). Groove generation and coalescence on a large-scale laboratory fault. *AGU Advances*, 1. doi:10.1029/2020AV000184
- Byerlee, J. (1967). Frictional characteristics of granite under high confining pressure. *Journal of Geophysical Research*, 72(14), 3639-3648. doi:10.1029/JZ072i014p03639
- Cappa, F., Scuderi, M., Collettini, C., Guglielmi, Y., & Avouac, J.-P. (2019). Stabilization of fault slip by fluid injection in the laboratory and in situ. *Science Advances*, 5(3). doi:10.1126/sciadv.aau4065
- Cattania, C., & Segall, P. (2021). Precursory Slow Slip and Foreshocks on Rough Faults. *Journal of Geophysical Research: Solid Earth*, 126(4). doi:10.1029/2020JB020430
- Cebry, S., & McLaskey, G. (2021). Seismic swarms produced by rapid fluid injection into a low permeability laboratory fault. *Earth and Planetary Science Letters*, 557. doi:10.1016/j.epsl.2020.116726
- Dieterich, J. (1992). Earthquake nucleation on faults with rate-and state-dependent strength. *Tectonophysics*, 211(1-4), 115-134. doi:10.1016/0040-1951(92)90055-B
- Dieterich, J. H. (1978). Time-Dependent Friction and the Mechanics of Stick-Slip. In J. D. Byerlee, & M. Wyss, *Rock Friction and Earthquake Prediction. Contributions to Current Research in Geophysics (CCRG)*. Birkhäuser, Basel.
- Ellsworth, W. (2013). Injection-Induced Earthquakes. *Science*, 341(6142). doi:10.1126/science.1225942
- Galis, M., Ampuero, J., Mai, P., & Cappa, F. (2017). Induced seismicity provides insight into why earthquake ruptures stop. *Science Advances*, 3(12). doi:10.1126/sciadv.aap7528
- Garagash, D., & Germanovich, L. (2012). Nucleation and arrest of dynamic slip on a pressurized fault. *Journal of Geophysical Research B: Solid Earth*, 117(10). doi:10.1029/2012JB009209
- Goebel, T. H., & Brodsky, E. E. (2018). The spatial footprint of injection wells in a global compilation of induced earthquake

sequences. *Science*, 361 (6405), 899-904. doi:10.1126/science.aat5449

Guglielmi, Y., Cappa, F., Avouac, J., Henry, P., & Elsworth, D. (2015a). Seismicity triggered by fluid injection-induced aseismic slip. *Science*, 348(6240), 1224-1226. doi:10.1002/2015JB012158

Guglielmi, Y., Elsworth, D., Cappa, F., Henry, P., Gout, C., Dick, P., & Durand, J. (2015b). In situ observations on the coupling between hydraulic diffusivity and displacements during fault reactivation in shales. *Journal of Geophysical Research: Solid Earth*, 120(11), 7729-7748. doi:10.1126/science.aab0476

Hubbert, M., & Rubey, W. (1959). Role of fluid pressure in mechanics of overthrust faulting. *Bulletin of the Geological Society of America*, 70, 115-166. doi:10.1130/0016-7606

Ida, Y. (1972). Cohesive force across the tip of a longitudinal-shear crack and Griffith's specific surface energy. *Journal of Geophysical Research*, 77(20), 3796-3805. doi:10.1029/jb077i020p03796

Ikari, M., Saffer, D., & Marone, C. (2009). Frictional and hydrologic properties of clay-rich fault gouge. *Journal of Geophysical Research: Solid Earth*, 114(5). doi:10.1029/2008JB006089

Kammer, D., Radiguet, M., Ampuero, J., & Molinari, J. (2015). Linear elastic fracture mechanics predicts the propagation distance of frictional slip. *Tribology Letters*, 57(3). doi:10.1007/s11249-014-0451-8

Kanamori, R., & Rivera, L. (2006). Energy Partitioning During an Earthquake. In *Earthquakes: Radiated energy and the physics of faulting*. *Geophysical Monograph Series. No. 170* (pp. 3-13). Washington, DC: American Geophysical Union. Retrieved from <https://resolver.caltech.edu/CaltechAUTHORS:20110629-112907012>

Kaneko, Y., Nielsen, S., & Carpenter, B. (2016). The onset of laboratory earthquakes explained by nucleating rupture on a rate-and-state fault. *Journal of Geophysical Research: Solid Earth*, 121(8), 6071-6091. doi:10.1002/2016JB013143

Kato, N., Yamamoto, K., Yamamoto, H., & Hirasawa, T. (1992). Strain-rate effect on frictional strength and the slip nucleation process. *Tectonophysics*, 211(1-4), 269-282. doi:10.1016/0040-1951(92)90064-D

Ke, C., McLaskey, G., & Kammer, D. (2018). Rupture Termination in Laboratory-Generated Earthquakes. *Geophysical Research Letters*, 45(23), 12,784-12,792. doi:10.1029/2018GL080492

Ke, C., McLaskey, G., & Kammer, D. (2021). The earthquake arrest zone. *Geophysical Journal International*, 224(1), 581-589. doi:10.1093/gji/ggaa386

Keranen, K., Savage, H., Abers, G., & Cochran, E. (2013). Potentially induced earthquakes in Oklahoma, USA: Links between wastewater injection and the 2011 Mw 5.7 earthquake sequence. *Geology*, 41(6), 699-702. doi:10.1130/G34045.1

Kim, K., Ree, J., Kim, Y., Kim, S., Kang, S., & Seo, W. (2018). Assessing whether the 2017 Mw5.4 Pohang earthquake in South Korea was an induced event. *Science*, 360(6392), 1007-1009. doi:10.1126/science.aat6081

Kranz, R. L., Frankel, A. D., Engelder, T., & Scholz, C. H. (1979). The Permeability of Whole and Jointed Barre Granite. *Int. J. Rock Mech. Min. Sci. & Geomech. Abstr.*, 16(4), 225-234. doi:10.1016/0148-9062(79)91197-5

Langenbruch, C., Ellsworth, W., Woo, J., & Wald, D. (2020). Value at Induced Risk: Injection-Induced Seismic Risk From Low-Probability, High-Impact Events. *Geophysical Research Letters*, 47(2). doi:10.1029/2019GL085878

Larochelle, S., Lapusta, N., Ampuero, J., & Cappa, F. (2021). Constraining Fault Friction and Stability With Fluid-Injection Field Experiments. *Geophysical*

Research Letters, 48(10). doi:10.1029/2020GL091188

Leeman, J. R., Saffer, D. M., Scuderi, M. M., & Marone, C. (2016). Laboratory observations of slow earthquakes and the spectrum of tectonic fault slip modes. *Nature Communications*, 7:11104. doi:10.1038/ncomms11104

Li, Z., Elsworth, D., Wang, C., Boyd, L., Frone, Z., Metcalfe, E., . . . McClure, M. (2021). Constraining maximum event magnitude during injection-triggered seismicity. *Nature Communications*, 12(1). doi:10.1038/s41467-020-20700-4

Madariaga, R. (1976). Dynamic of an expanding, circular fault. *Bulletin of the Seismological Society of America*, 66(3), 639-666. doi:10.1785/BSSA0660030639

McLaskey, G. (2019). Earthquake Initiation From Laboratory Observations and Implications for Foreshocks. *Journal of Geophysical Research: Solid Earth*, 124(12), 12882-12904. doi:10.1029/2019JB018363

McLaskey, G., & Kilgore, B. (2013). Foreshocks during the nucleation of stick-slip instability. *Journal of Geophysical Research: Solid Earth*, 118(6), 2982-2997. doi:10.1002/jgrb.50232

McLaskey, G., & Yamashita, F. (2017). Slow and fast ruptures on a laboratory fault controlled by loading characteristics. *Journal of Geophysical Research: Solid Earth*, 122(5), 3719-3738. doi:10.1002/2016JB013681

Passelègue, F., Brantut, N., & Mitchell, T. (2018). Fault Reactivation by Fluid Injection: Controls From Stress State and Injection Rate. *Geophysical Research Letters*, 45(23), 12,837-12,846. doi:10.1029/2018GL080470

Raleigh, C., Healy, J., & Bredehoeft, J. (1976). An Experiment in Earthquake Control at Rangely, Colorado. *Science*, 191(4233), 1230-1237. doi:10.1126/science.191.4233.1230

Rice, J. (1993). Spatio-temporal Complexity of Slip on a Fault. *Journal of Geophysical Research*, 98(B6), 9885-9907. doi:10.1029/93JB00191

Rogers, G., & Dragert, H. (2003). Episodic tremor and slip on the Cascadia subduction zone: the chatter of silent slip. *Science*, 300(5627), 1942-1943. doi:10.1126/science.300.5627.1942

Ross, Z. E., Cochran, E. S., Trugman, D. T., & Smith, J. D. (2020). 3D fault architecture controls the dynamism of earthquake swarms. *Science*, 368(6497), 1357. doi:10.1126/science.abb0779

Scuderi, M., & Collettini, C. (2018). Fluid Injection and the Mechanics of Frictional Stability of Shale-Bearing Faults. *Journal of Geophysical Research: Solid Earth*, 123(10), 8364-8384. doi:10.1029/2018JB016084

Shelly, D. R., Hill, D. P., Massin, F., Farrell, J., Smith, R. B., & Taira, T. (2013). A fluid-driven earthquake swarm on the margin of the Yellowstone caldera. *Journal of Geophysical Research: Solid Earth*, 118, 4872-4886. doi:10.1002/jgrb.50362

Svetlizky, I., & Fineberg, J. (2014). Classical shear cracks drive the onset of dry frictional motion. *Nature*, 509(7499), 205-208. doi:10.1038/nature13202

Uenishi, K., & Rice, J. (2003). Universal nucleation length for slip-weakening rupture instability under nonuniform fault loading. *Journal of Geophysical Research: Solid Earth*, 108(B1). doi:10.1029/2001JB001681

Villiger, L., Gischig, V., Kwiitek, G., Krietsch, H., Doetsch, J., Jalali, M., . . . Wiemer, S. (2021). Metre-scale stress heterogeneities and stress redistribution drive complex fracture slip and fracture growth during a hydraulic stimulation experiment. *Geophysical Journal International*, 225(3), 1689-1703. doi:10.1093/gji/ggab057

Wang, L., Kwiitek, G., Rybacki, E., Bonnelye, A., Bohnhoff, M., & Dresen, G. (2020). Laboratory Study on Fluid-Induced Fault Slip Behavior: The Role of Fluid Pressurization

Rate. *Geophysical Research Letters*, 47(6). doi:10.1029/2019GL086627 Wu, B., & McLaskey, G. (2019). Contained Laboratory Earthquakes Ranging From Slow to Fast. *Journal of Geophysical Research: Solid Earth*, 124(10), 10270-10291. doi:10.1029/2019JB017865 Wynants-Morel, N., Cappa, F., DeBarros, L., & Ampuero, J.-P. (2020). Stress perturbation from aseismic slip drives the seismic front during fluid injection into a permeable fault. *JGR Solid Earth*, 125(7). doi:10.1029/2019JB019179 Yang, Y., & Dunham, E. M. (2021). Effect of Porosity and Permeability Evolution on Injection-Induced Aseismic Slip. *JGR Solid Earth*, 126(7). doi:10.1029/2020JB021258

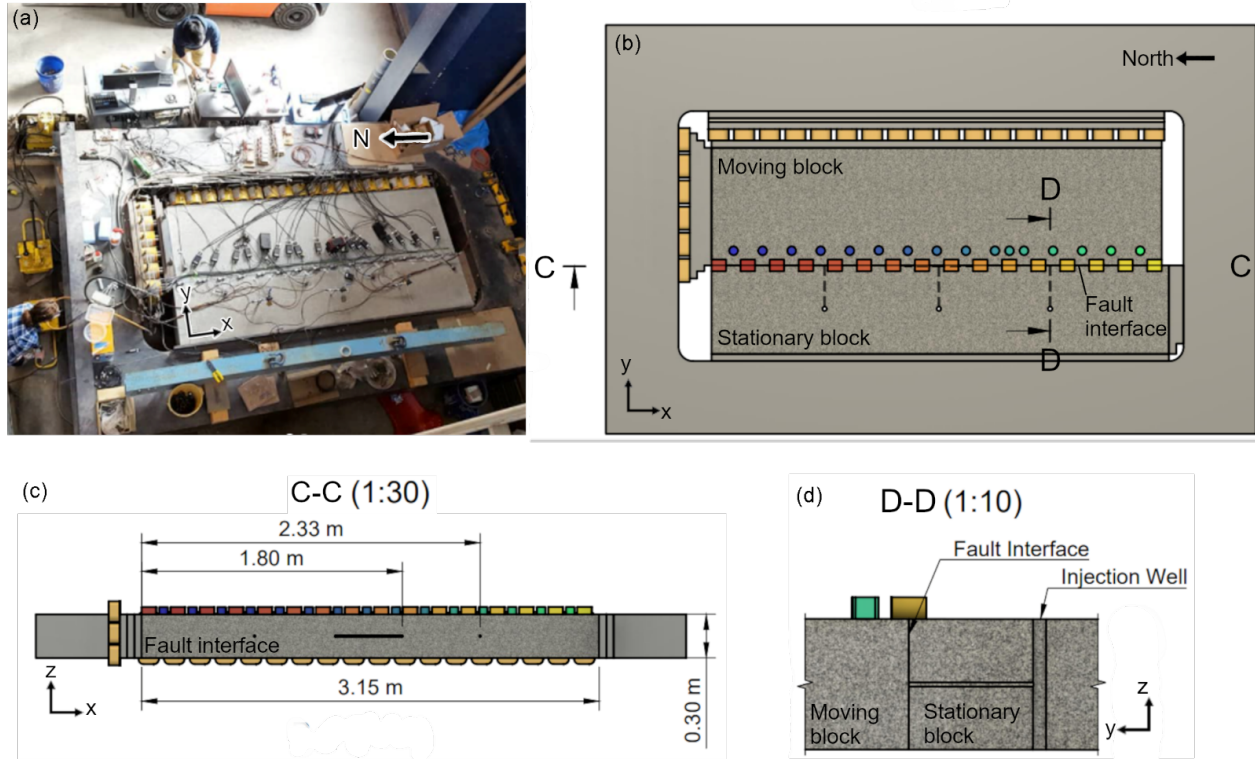


Figure 1. Schematic of Cornell 3 m biaxial apparatus and samples. (a) Photograph of apparatus. (b) Plan view of apparatus. Colored squares indicate slip sensors and circles indicate strain gauges. Sensors are numbered 1 – 16 from north to south (left to right in schematic). (c) Section B-B shows a cross section of the sample face. During experiments, water was injected through the hole located 2.33 m from the forcing end. On-fault water pressure was measured both in the injection well and in the trough located 1.8 m from the forcing end. (d) Cross section of the stationary block shows the injection well. Water was injected directly onto the fault interface.

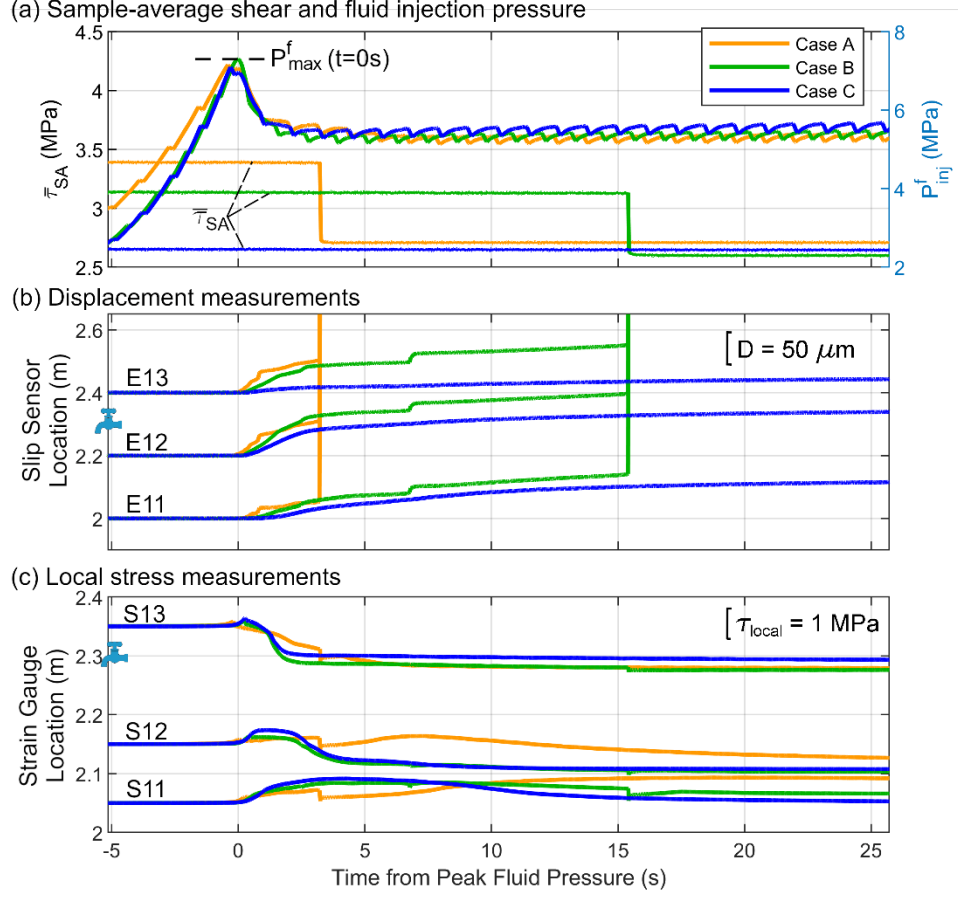


Figure 2. Results for Case A (high $-\sigma_0$, orange), B (moderate $-\sigma_0$, green), and C (low $-\sigma_0$, blue) overlaid for comparison. Data is synchronized based on peak injection fluid pressure, P_{max}^f . (a) fluid pressure measured in the injection well and sample-average shear stress, both measured by hydraulic sensors. Oscillations in fluid pressure are due to HPLC pump strokes. (b) displacement measurements, D , from three slip sensors, offset by their location along the fault relative to the forcing end. (c) local stress measurements, τ_{local} from three strain gauges, offset by their location along the fault. Blue faucet symbol in (b) and (c) indicates injection point. Dynamic slip events are indicated by a sudden increase in D and, in cases that rupture the forcing end of the sample, a sudden decrease in $\bar{\tau}_{SA}$. Aseismic slip is indicated by a gradual increase in D and a gradual change in τ_{local} .

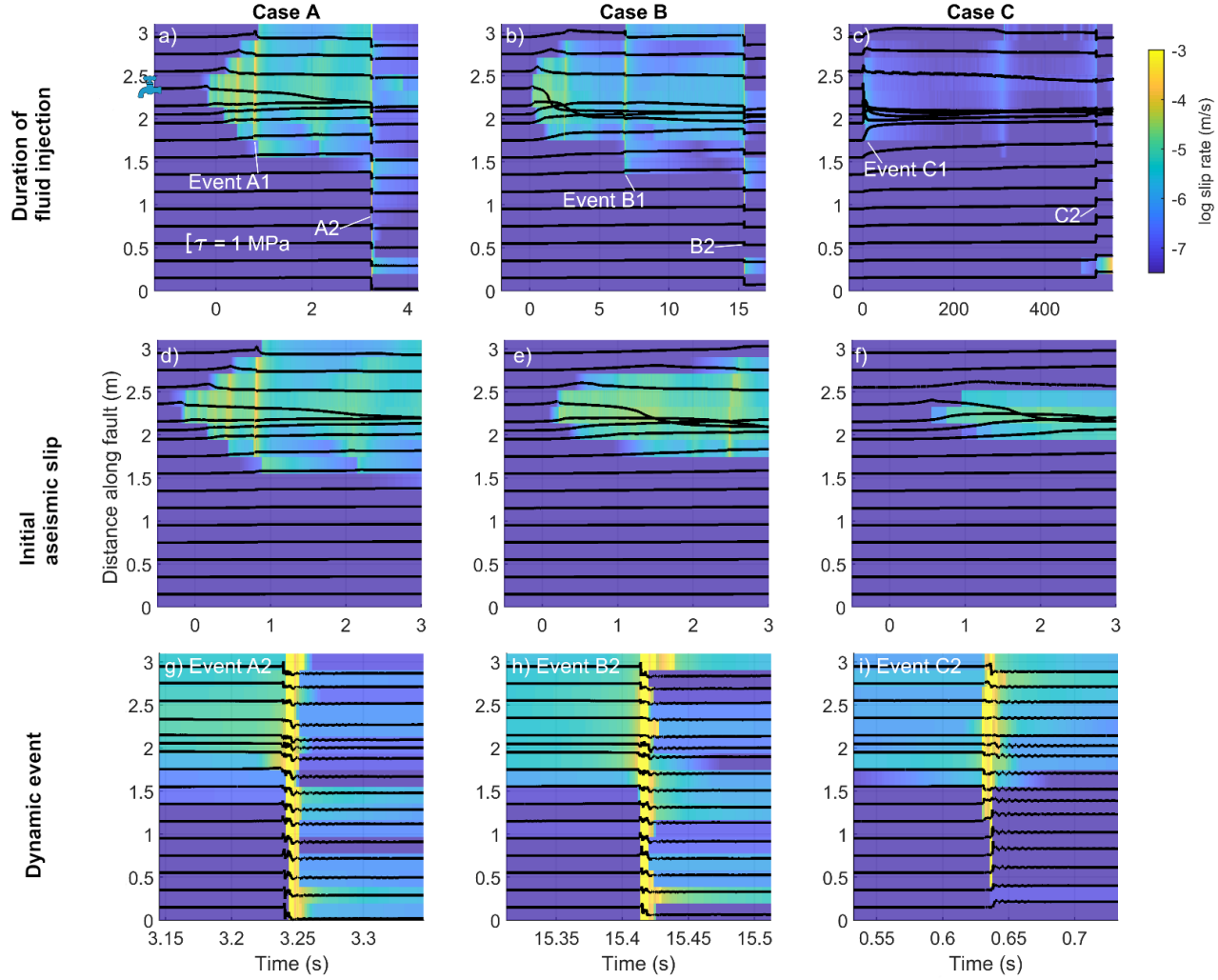


Figure 3. Local shear stress and slip rate as a function of time and distance along the fault for Cases A, B, and C (vertical columns). Local shear stress is shown by black lines. Lines are offset along the y-axis by sensor location along the fault. Slip rate, based on displacement sensor measurements, is shown as a colormap. Top panels show long term trends at different time scales. Middle panels show the first 3 seconds of aseismic slip in each case. Bottom panels show a zoom in of a single dynamic event with uniform time scales for each Case. Blue faucet in panel a indicates the location of fluid injection.

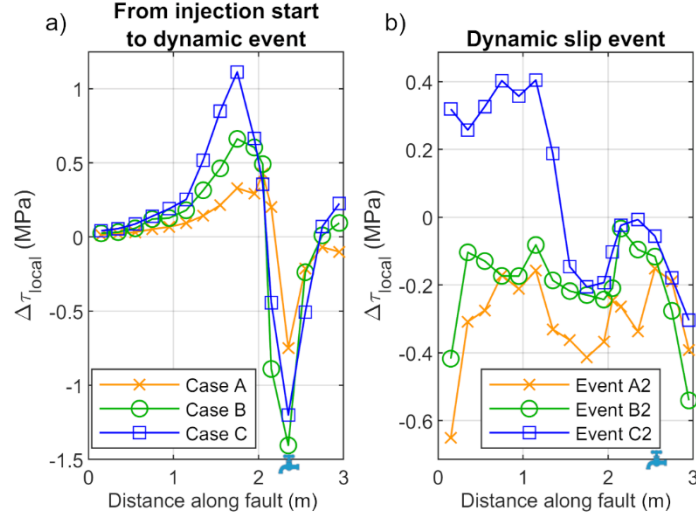


Figure 4. a) Change in shear stress from the start of fluid injection to the initiation of a dynamic event as a function of distance along the fault. Fluid is injected at 2.3 m. b) Change in local shear stress from a 1 second window centered around the largest fluid-triggered dynamic slip event in each Case. In Case A and B this event ruptured the entire fault, which resulted in a negative stress change over the entire fault, while Case C only ruptured from 0.4 m to 3 m, which resulted in positive stress change around the locked patch.

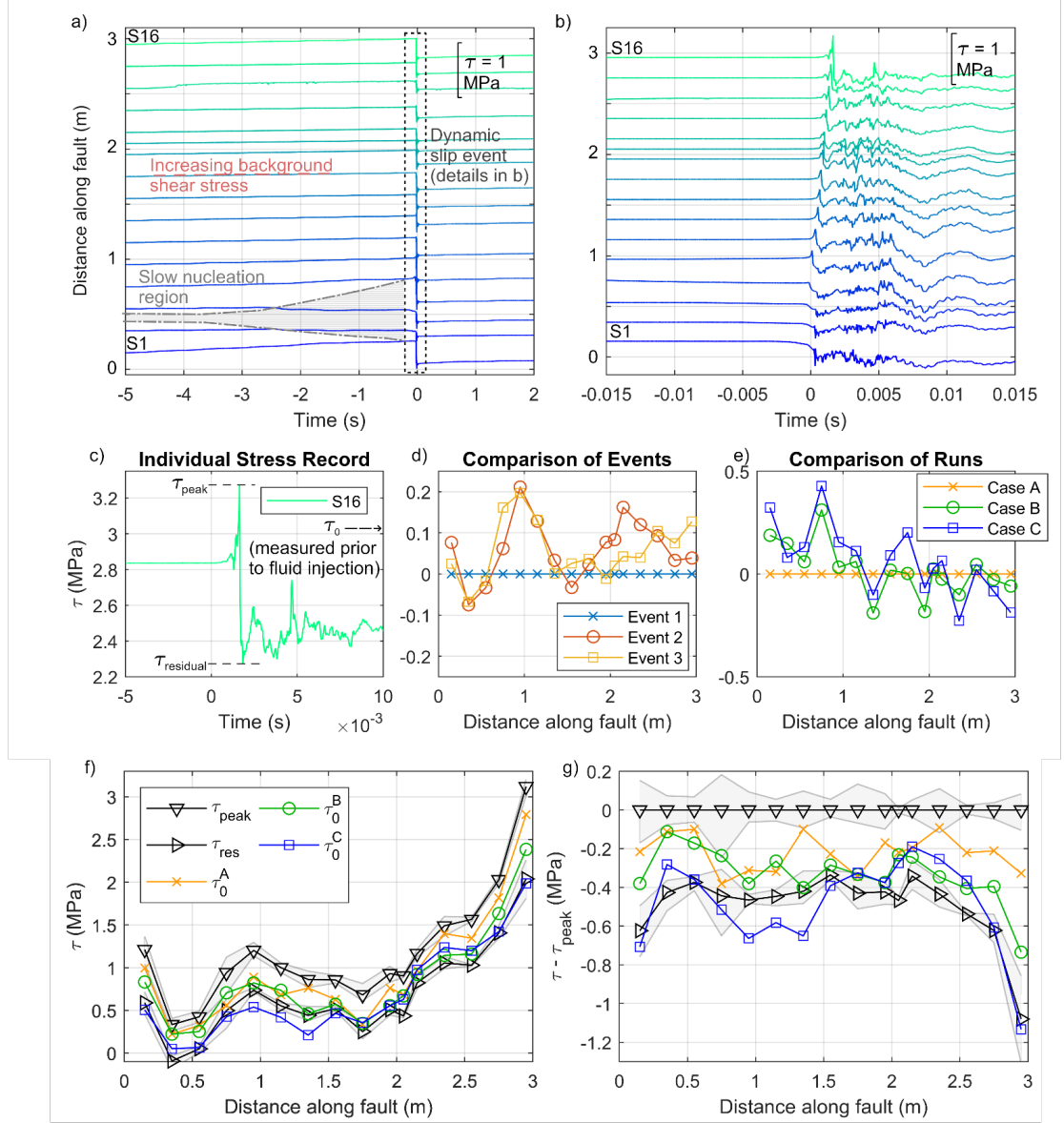
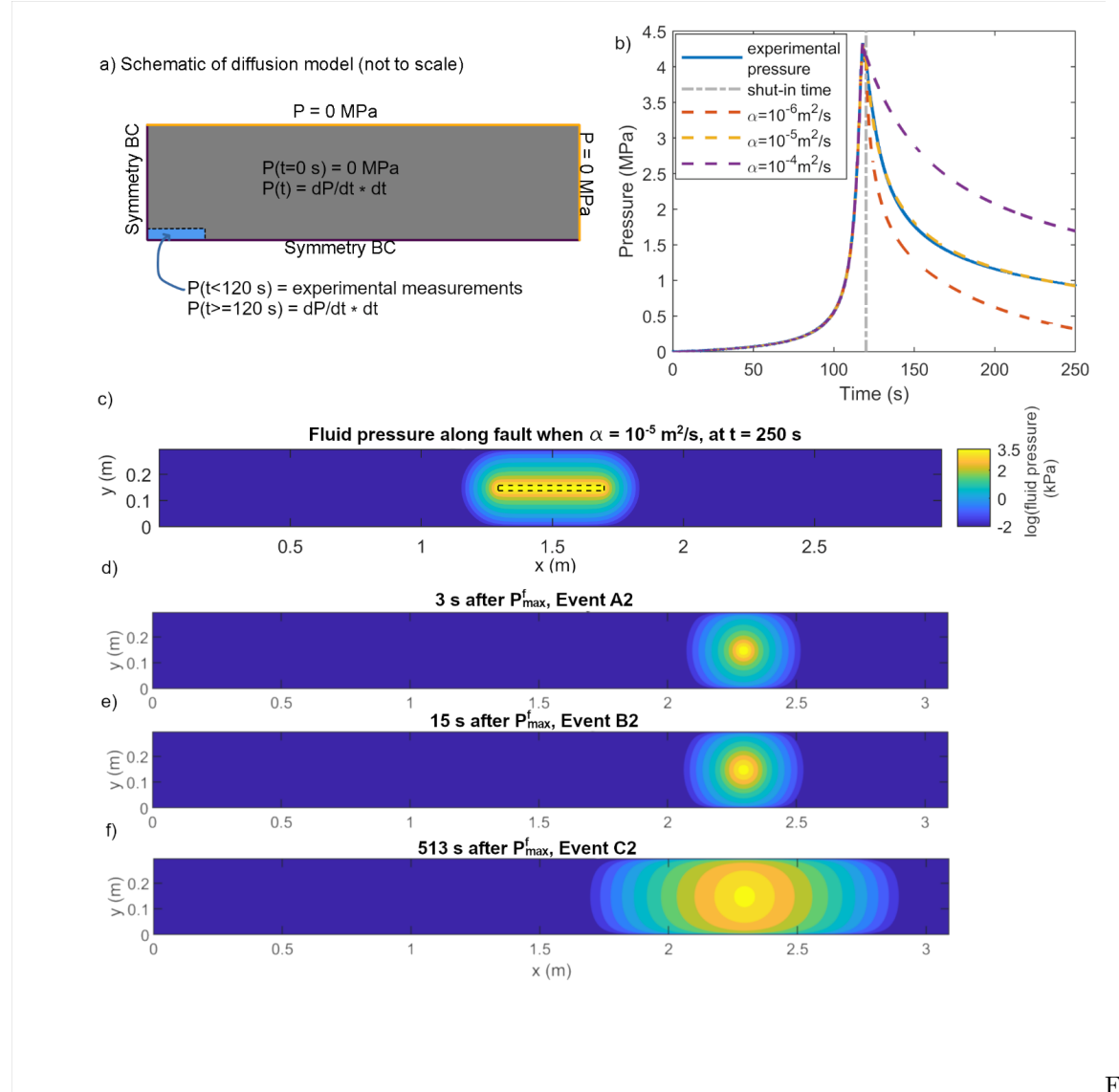


Figure 5. (a) and (b) Shear stress as measured by strain gauge pairs at 16 points along the fault. Traces are offset by the gauge location along the fault for clarity. Measurements show a shear-triggered event which nucleated 50 cm from the forcing end and ruptured the entire length of the fault. (c) close up of a strain gauge S16 measurements during the shear-triggered event shown in (a) and (b) to demonstrate how τ_{peak} and τ_{residual} were chosen at every gauge location. (d) τ_{peak} as a function of distance along the fault for 3 different shear-

triggered events from Case A. (e) Average τ_{peak} from Case A, B, and C. (f) and (g) τ_0 for Case A, B, and C compared to the average τ_{peak} and τ_{residual} across all events and all cases. Shaded gray region indicates range of τ_{peak} and τ_{residual} values. (f) shows the shear stress values normalized by the starts of the experiment. (g) shows the same data normalized by τ_{peak} for each case.



Figure

6. 2D diffusion model used to estimate the diffusivity of the fault. a) Schematic of the diffusion model shows the fault face. The injection well, shown in blue, has experimental pressure measurements imposed for the first 120 s, then was free after 120 s. A symmetry boundary condition was imposed at $x = 0$ m and

$y = 0$ m. The edges of the fault ($x = 1.5$ m and $y = 0.14$ m), which were open to atmospheric pressure during the experiment, were modeled as free surfaces where $P^f = 0$ MPa. b) Modeled fluid pressure in the injection well as a function of time for three values of τ_0 compared with the experimental measurements. c) Pressure along the fault at $t = 250$ s. d-f) show fluid pressure during experiments based on pressure measured in the injection well and diffusion parameters determined by the shut-in test. The pressure scale for d-f) is the same as c). d) shows fluid pressure 3 s after P^f_{\max} when Event A2 occurred, e) shows fluid pressure 15 s after P^f_{\max} when Event B2 occurred, and f) shows fluid pressure 513 s after P^f_{\max} when Event C2 occurred.

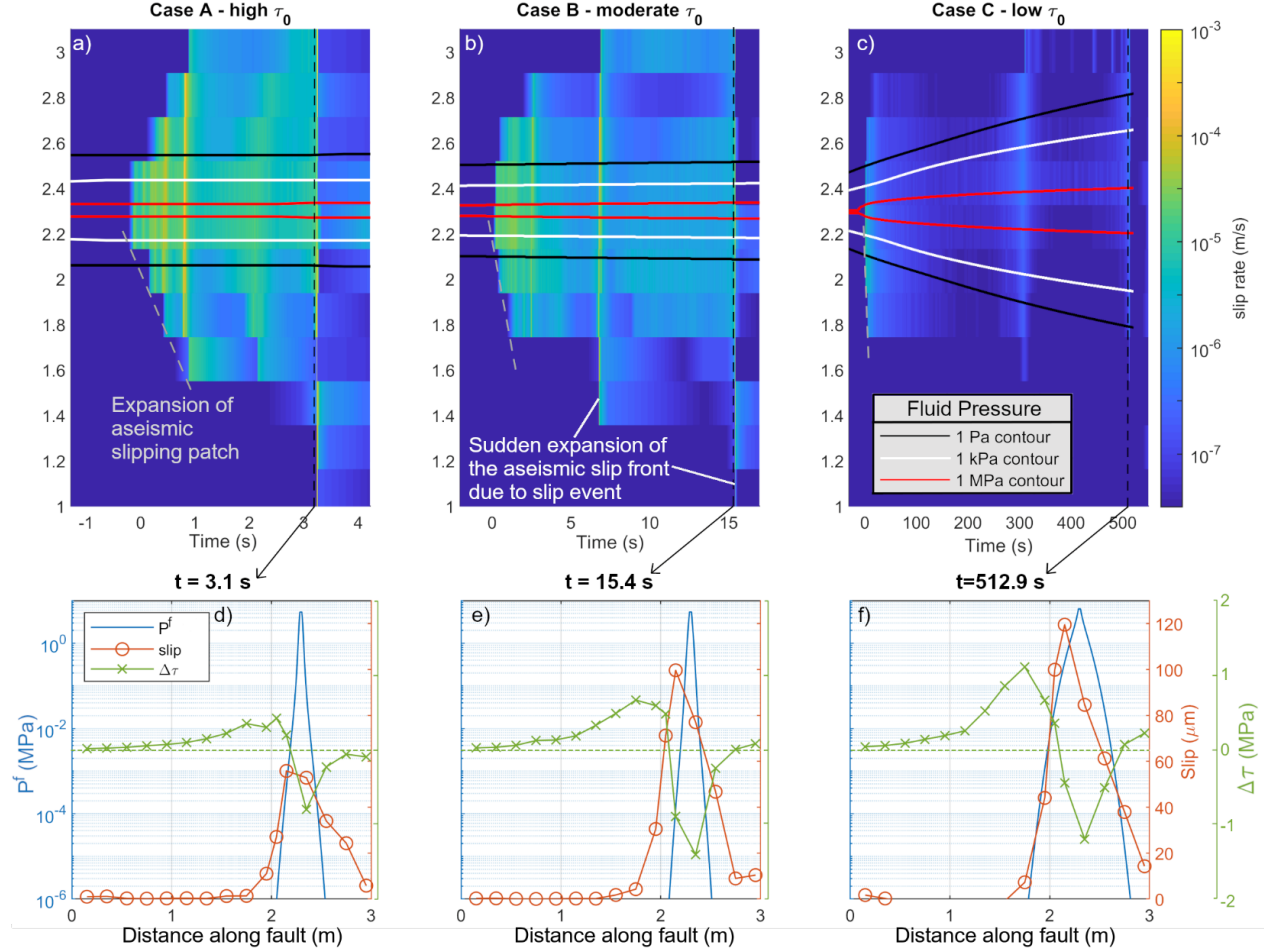


Figure 7. Slip rate and fluid pressurized region over the duration of fluid injection for Case A (a), Case B (b), and Case C (c). Fluid pressure contours are determined using a 2D diffusion model with $\kappa = 1 \times 10^{-5} \text{ m}^2/\text{s}$ and are shown

for 1 Pa, 1 kPa, and 1 MPa taken at the center of the fault (Figure 6, $y = 0.15$ m). The colormap shows log slip rate measured for the entire duration of fluid-triggered slip. d), e), and f) show modeled fluid pressure and measured slip and changes in shear stress on the same scale as a function of distance along the fault at a single time point. Time points are marked with a black dashed line in a), b), and c). Change in shear stress is the difference in shear stress from the start of injection to the time point shown.

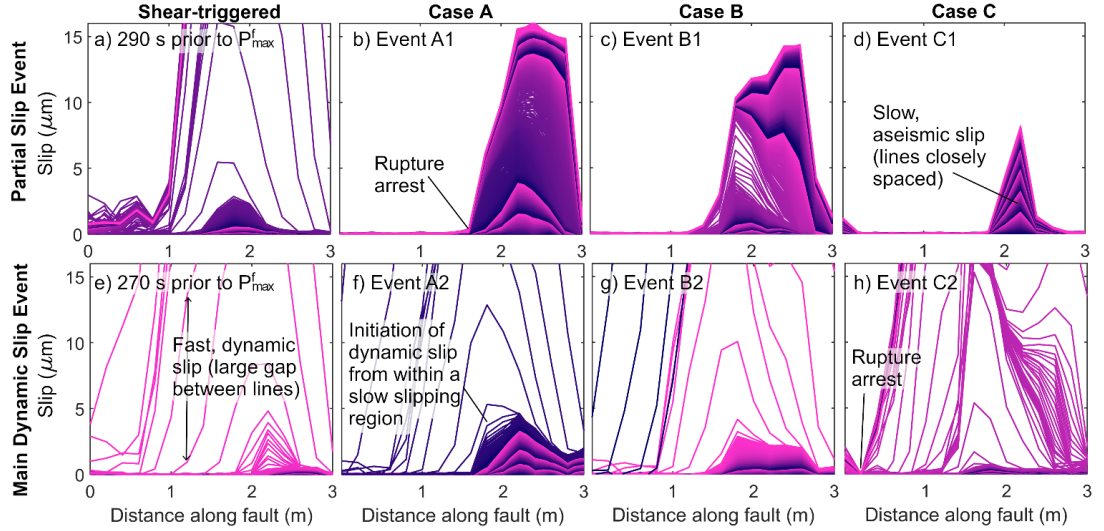


Figure 8. Slip as a function of distance and time for eight distinct slip events. The top row shows slip events that only ruptured a portion of the fault. The bottom row shows rupture events that ruptured the entire length of the fault (except for panel h, which was the largest fluid-triggered event in Case C). Each panel shows a 1 s window centered around individual slip events. Lines are plotted every 200 μ s and the color of the line cycles from dark purple to light pink every 0.1 s. a) and e) show events that are triggered solely by an increase in shear stress. These events were chosen since they initiated in a similar location to the fluid-triggered events. Fluid-triggered events are shown for Case A (b and f), Case B (c, g), and Case C (d, h).

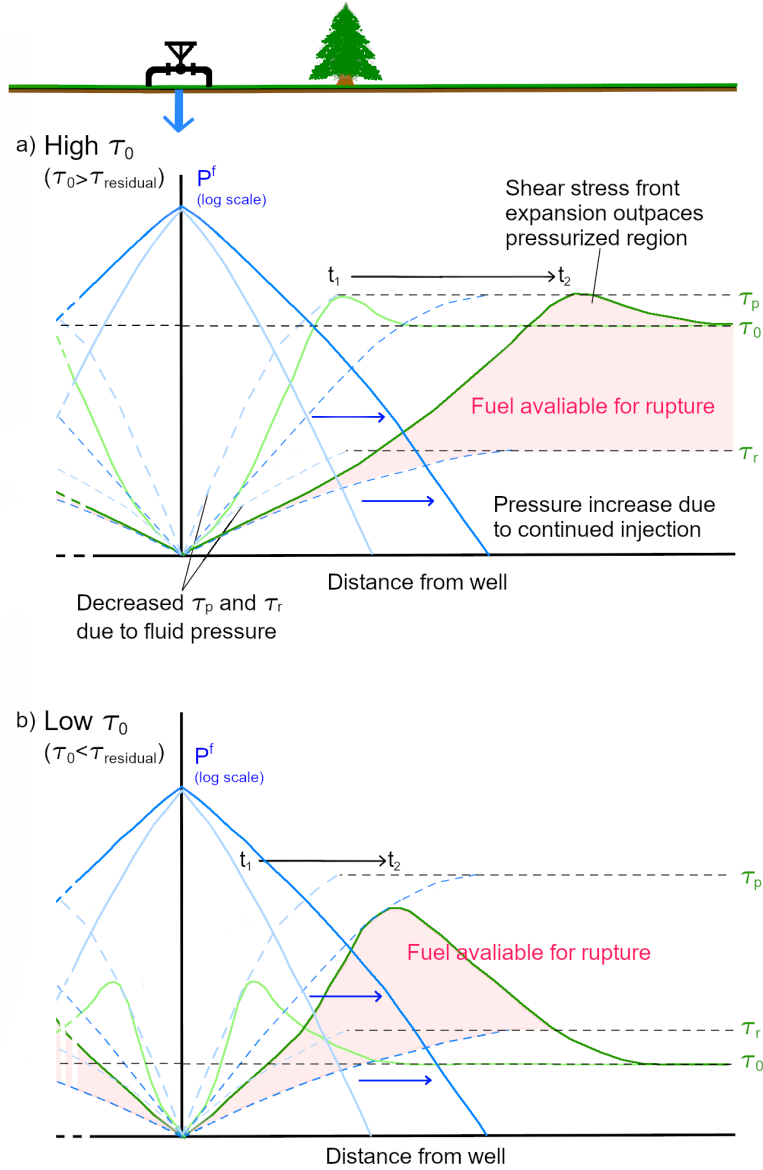


Figure 9. Schematic depicting the fuel available for dynamic rupture due to fluid injection and resulting aseismic slip under (a) high τ_0 conditions ($\tau_0 > \tau_{\text{residual}}$) and (b) low τ_0 conditions ($\tau_0 < \tau_{\text{residual}}$). Lighter blue and green lines depict approximate distributions of fluid pressure and shear stress, respectively,

at time t_1 , while darker blue and green lines correspond to t_2 . In the high τ_0 , there is fuel for fluid induced slip to rupture beyond the pressurized region. In the low τ_0 case, rupture is limited to the area affected by increased fluid pressure and induced aseismic slip.